INTERNATIONAL JOURNAL FOR NUMERICAL METHODS IN FLUIDS, VOL. 12, 985–1002 (1991)

A SEMI-IMPLICIT COLLOCATION METHOD: APPLICATION TO THERMAL CONVECTION IN 2D COMPRESSIBLE FLUIDS

SERGE GAUTHIER

CEA, Centre d'Etudes de Limeil-Valenton, F-94195 Villeneuve-St-Georges Cedex, France

SUMMARY

A semi-implicit pseudo-spectral collocation method using a third-order Runge–Kutta numerical scheme for the full Navier–Stokes equations is described. The Courant–Friedrichs–Lewy condition is overcome by the implicit handling of a diffusive term, as suggested by Harned and Kerner. All such terms are solved with an iterative scheme in the Fourier space. Simulation of thermal convection in 2D compressible fluids is made by expanding variables on a Fourier–Chebyshev basis. We give some examples of sub- and supersonic steady solutions in the case where the heat flux at the upper boundary is governed by a black body.

KEY WORDS Spectral methods Iterative methods Semi-implicit schemes Compressible convection

1. INTRODUCTION

Stability and transition to turbulence of compressible flows are subjects of growing interest. Such computations are usually performed within the framework of spectral methods owing to their high accuracy.[1,2] Direct numerical simulations of homogeneous isotropic turbulence have already been carried out by several authors. In that respect, Passot and Pouquet have developed a new artificial viscosity to perform supersonic compressible flow simulations in two dimensions.[3] To study the stability of compressible flows over a flat plate with one inhomogeneous direction, Erlebacher and Hussaini have carried out explicit 2D and 3D simulations with a fully explicit scheme.[4] For the study of the gravitational collapse of a star, Bonazzola and Marck wrote 2D and 3D pseudo-spectral codes for spherical geometry. They use semi-implicit schemes and a constant artificial viscosity to spread out the shock wave.[5] Compressible convection has also been simulated with spectral methods.[6,7]

In the particular case of thermal convection the Boussinesq equations have been widely used over the last 20 years. This approximation holds for a compressible fluid provided that the vertical extent of the fluid is small enough. In some situations, e.g. in stellar convection, the stratification of the fluid can no longer be ignored and we have to use the full Navier–Stokes equations. Since the pioneering work of Graham,[8] a number of papers have been devoted to the simulation of compressible convection within finite difference schemes.[9–11] Yamaguchi[11] studied the case of a constant inward heat flux at the bottom. He found supersonic solutions even at low Rayleigh numbers. High resolution of compressible convection in two and three dimensions has been carried out by Woodward *et al.*[12] They use a finite difference code based on the piecewise

0271-2091/91/100985-18$09.00

Received December 1989
Revised July 1990

parabolic method for the inviscid Euler equations. Dissipation of energy by numerical diffusion leads to time-dependent complex flows.

Owing to the very different time scales involved in a compressible flow, tens of thousands of time steps are required to achieve convergence in the compressible case while only thousands of time steps are needed in incompressible flow simulations. Indeed, the acoustic time scale may be 10^3–10^4 smaller than the viscous time scale. It is then necessary to use numerical schemes with a larger implicit part than those used in incompressible flow simulations.

In view of this, we have developed a 2D pseudo-spectral code for the full Navier–Stokes equations[7] which has been used so far to numerically simulate compressible Rayleigh–Bénard convection. A Fourier expansion is used in the horizontal direction. Expansion over the Chebyshev polynomials used in the vertical inhomogeneous direction leads to severe time step constraints owing to the high resolution on the boundaries. In order to overcome these constraints, the non-linear viscous and thermal diffusion terms are solved with an iterative method. In the first version of the code, diffusion terms in the vertical direction only were solved implicitly by an iterative method preconditioned by the time-independent Chebyshev approximation of the diffusion operator.

In this paper we present a more implicit version where convective terms are treated semi-implicitly and all diffusion terms are handled in the Fourier space with an iterative method preconditioned by the finite difference approximation of the diffusion operator. Both numerical schemes are used to compute sub- and supersonic steady state solutions obtained with a Robin boundary condition for the temperature and Neumann boundary conditions for the velocity.

Section 2 introduces the physical problem, Section 3 is devoted to details of the numerical scheme, and numerical applications are described in Section 4.

2. THE PHYSICAL PROBLEM

Motion takes place in a two-dimensional rectangular cavity of width L_x and height d. The x_2-axis is directed downwards so that the gravitation, represented by the vector $\mathbf{g}=(0, 0, g)$, is positive along this direction. The fluid layer extends from $x_{2,0}$ to $x_{2,0}+d$.

The evolution equations for a compressible, viscous, thermally conducting gas are as follows:

$$\frac{\partial \rho}{\partial t}+\frac{\partial \rho u_i}{\partial x_i}=0, \tag{1}$$

$$\frac{\partial \rho u_i}{\partial t}+\frac{\partial \rho u_i u_j}{\partial x_j}=-\frac{\partial P}{\partial x_i}+\frac{\partial \sigma_{ij}}{\partial x_j}-\rho g_i, \tag{2}$$

$$\frac{\partial \rho E}{\partial t}+\frac{\partial u_j(\rho E+P)}{\partial x_j}=\frac{\partial \sigma_{ij}u_j}{\partial x_i}+\frac{\partial}{\partial x_i}K\frac{\partial T}{\partial x_i}, \tag{3}$$

where E is the total energy defined by

$$E=\tfrac{1}{2}(u_1^2+u_2^2)+e-gx_2, \tag{4}$$

σ_{ij} is the viscous stress tensor given by

$$\sigma_{ij}=\mu\left(\frac{\partial u_i}{\partial x_j}+\frac{\partial u_j}{\partial x_i}-\frac{2}{3}\delta_{ij}\frac{\partial u_l}{\partial x_l}\right) \tag{5}$$

and $i, j, l=1, 2$. The Stokes relation between the first and second viscosity coefficients has been

used. This set of equations is closed by the equations of state for a monatomic perfect gas:

$$P = R_* \rho T, \qquad e = C_v T. \tag{6}$$

P, ρ, T and e are the pressure, the density, the temperature and the internal energy respectively; the u_i are the components of the velocity. The thermal conductivity and the dynamic viscosity coefficients are taken as constants. R_* is the gas constant and C_v the specific heat at constant volume.

We use free slip boundary conditions for the velocity and a Robin boundary condition for the temperature. This set of boundary conditions is a reasonable approximation for stellar convection zones. The boundary conditions for the velocity are as

$$u_2 = 0 \quad \text{and} \quad \frac{\partial u_1}{\partial x_2} = 0 \quad \text{at } x_2 = x_{2,0},\ x_{2,0} + d. \tag{7}$$

The upper boundary condition for the temperature is obtained by imposing the heat flux at the upper boundary to be fixed by the radiative flux of a black body,

$$K \frac{dT}{dx_2} = \sigma^{sb} T^4, \tag{8}$$

where σ^{sb} is the Stefan–Boltzmann constant. Taking into account the fluctuations of the thermal conductivity up to first order with respect to the density and the temperature and linearizing equation (8), we get the following relation at the upper boundary:

$$\frac{1}{\sigma^{sb}} \frac{d\theta}{dx_2} + \frac{1}{K_0} \frac{dK}{d\rho} \rho + \frac{1}{K_0} \frac{dK}{d\theta} \theta = 4\theta, \tag{9}$$

where ρ and θ are the fluctuations of density and temperature respectively. Assume then the following form for the thermal conductivity $K(\rho, \theta)$ of the black body:

$$K(\rho, \theta) \propto \frac{(\bar{T} + \theta)^3}{(\bar{\rho} + \rho')}, \quad \text{with } K_0 = K(0, 0), \tag{10}$$

where $\bar{\rho}$ and $\bar{T}$ are some basic state of density and temperature respectively. Equation (9) then leads to the following inhomogeneous time-dependent Robin-type boundary conditions for the temperature fluctuations:

$$\frac{1}{S_f} \frac{d\theta}{dz}(x, Z^{-1}, t) - \theta(x, Z^{-1}, t) = \rho(x, Z^{-1}, t) \quad \text{at the top layer}$$

$$\theta(x, Z^{-1} + 1, t) = 0 \qquad \text{at the bottom layer,} \tag{11}$$

where S_f is the Stefan number defined by $S_f = \sigma^{sb} T^3 d / K_0$.

Periodic boundary conditions are used in the horizontal direction for all variables.

In equation (11) we have used dimensionless variables by rescaling length, time, density and temperature as d, $d^2 \rho(x_{2,0})/\mu$, $\rho(x_{2,0})$ and $T(x_{2,0})$ respectively. Moreover, we have defined $x = x_1/d$ and $z = x_2/d$.

With these boundary conditions in the z-direction, the static state obtained by setting $\partial/\partial t = 0$ and $u_i = 0$ in equations (1)–(3) is

$$\bar{T}(z) = S_f z + 1 - S_f Z^{-1}, \tag{12a}$$

$$\bar{\rho}(z) = (S_f z + 1 - S_f Z^{-1})^m, \tag{12b}$$

$$\bar{P}(z) = (S_f z + 1 - S_f Z^{-1})^{m+1}, \tag{12c}$$

where the dimensionless co-ordinate z goes from Z^{-1} to $Z^{-1}+1$, with $Z=d/x_{2,0}$. To be consistent with Dirichlet boundary conditions, we have kept the parameter Z.[7-10] However, in this case the stratification parameter is S_f and the index of the polytrope is

$$m=\frac{g}{R_*\beta_0}-1, \quad \text{where } \beta_0=T(z_0+d)-T(z_0). \tag{13}$$

The two-dimensional compressible convection problem is characterized by six dimensionless parameters, namely the aspect ratio A, the Prandtl number Pr, the ratio of specific heats γ, the polytropic index m, the Stefan number S_f and the Reyleigh number Ra. The parameters Pr and γ are given by the thermodynamical properties of the fluid. The Stefan number measures the magnitude of the radiative diffusion with respect to the thermal conductivity and the stratification. The Rayleigh number measures the degree of instability. Their expressions are

$$A=\frac{L_x}{d}, \qquad Pr=\frac{\mu C_p}{K}, \qquad Z=\frac{d}{z_0}, \qquad \gamma=\frac{C_p}{C_v},$$

$$Ra=\frac{gd^4}{T_U}\left(\frac{T_L-T_U}{d}-\frac{g}{C_p}\right)\Big/\left(\frac{K}{\rho_U C_p}\frac{\mu}{\rho_U}\right),$$

where the subscripts L and U refer to the lower and upper layer boundaries.

3. DESCRIPTION OF THE PSEUDO-SPECTRAL CODE

Density, velocity and total energy are expanded over a Fourier–Chebyshev basis as

$$u(x, z, t)=\sum_{l=-N/2}^{l=N/2-1}\sum_{m=0}^{M} u_{lm}(t)\exp(-2i\pi lx/L_x)T_m(2z), \tag{14}$$

where T_m is the Chebyshev polynomial of degree m and L_x is the horizontal periodicity.

We use a collocation method where spatial derivatives are computed in the spectral space and non-linear products are performed in the physical space at the grid points

$$x_i=iL_x/N, \quad i=0, 1, \ldots, N-1, \tag{15}$$

$$z_j=Z^{-1}+\frac{1}{2}\left[1+\cos\left(\pi\frac{M-j}{M}\right)\right], \quad j=0, 1, \ldots, M. \tag{16}$$

Time marching is also performed in the physical space by means of a finite difference technique. As already stated, a simple numerical scheme consists of the Adams–Bashforth predictor of order two and the third-order Adams–Moulton corrector for all but the vertical diffusion terms. These terms are handled by an iterative procedure preconditioned by the time-independent Chebyshev approximation of the diffusion operator. This spectral preconditioning appears to be very efficient as regards the CPU time and the number of iterations needed to achieve a given accuracy. In this approach, however, the time step obeys the CFL condition

$$\Delta t_{CFL}=c\min_{grid}\left(\frac{\Delta x}{|u|+c_s}, \pi\frac{\Delta z}{|v|+c_s}\right), \tag{17}$$

where c is a constant that depends on the numerical scheme. It is then of interest to test more implicit numerical methods in order to overcome this constraint.

3.1. The semi-implicit numerical scheme: a model equation

As pointed out in Reference 13, the key idea of semi-implicit numerical schemes lies in the recognition of the source term that produces numerical instability. A simple approximation, e.g. linear, may then be treated implicitly. Harned and Kerner[14] have applied this idea to the magnetohydrodynamics equations within the finite difference framework. They notice that fast modes are described by a wave equation obtained from linearizing the Euler equation and the energy equation:

$$\frac{\partial^2 u}{\partial t^2} = \frac{\gamma P_0}{\rho_0} \nabla(\nabla \cdot u), \tag{18}$$

where v is the x-component of the velocity and P_0 is the pressure. Consequently, the term $A_0^2 \Delta t^2 \nabla (\nabla \cdot u)$ is added to both sides of the velocity equations and solved implicitly with a second-order Runge–Kutta numerical scheme. A_0 is a constant and Δt is the time step. Unconditional stability is ensured if all eigenvalues lie within the unit circle. This occurs for

$$A_0^2 > \frac{\gamma P_0}{16 \rho_0} (1 + 2\theta)^2, \tag{19}$$

where θ is the Crank–Nicholson parameter chosen close to $\frac{1}{2}$.

If we now use the Navier–Stokes equation by adding a viscous term such as $v \partial^2 / \partial x^2$ to the velocity equation, equation (18) may be rewritten as

$$U^{n+1} = A U^n, \tag{20}$$

where $U^\dagger = (u, P)^\dagger$ and

$$A = \begin{pmatrix} 1 - \theta \dfrac{\alpha}{Y} - \dfrac{v k^2 \Delta t}{Y} & -\dfrac{\Delta t i k}{\rho} \dfrac{1}{Y} \\ -\dfrac{\Delta t i k}{2} \gamma P_0 \left(2 - \theta \dfrac{\alpha}{Y} \right) & 1 - \dfrac{\alpha}{2Y} \end{pmatrix}.$$

A Fourier discretization has been used, $\alpha = \Delta t^2 k^2 \gamma P_0 / \rho_0$ and $Y = 1 + \Delta t^2 k^2 A_0^2$. The condition on A_0 now reads

$$A_0^2 > \frac{1}{16} \frac{\rho_0}{\gamma P_0} (1 + 2\theta)^2 + \frac{1}{\Delta t^2} \frac{v^2}{4} \frac{\rho_0}{\gamma P_0} + \frac{1}{\Delta t} v (2\theta - 1). \tag{21}$$

Combination of a second-order Runge–Kutta numerical scheme with a Chebyshev approximation is unfortunately known to be weakly stable. We therefore turned to a semi-implicit third-order Runge–Kutta scheme (RK3) in a low-storage formulation.[1, 15] This scheme reads

$$\frac{\partial u}{\partial t} \doteq \mathrm{F}(u) + G(u), \tag{22a}$$

where the terms $F(u)$ and $G(u)$ are respectively treated explicitly and implicitly:

$$H_1 = \Delta t F(u^n), \tag{22b}$$

$$\mathscr{D} u_1 = \mathscr{D} u^n + \tfrac{1}{3} H_1 + \tfrac{1}{6} \Delta t (G^n + G_1), \tag{22c}$$

$$H_2 = \Delta t F(u_1) - \tfrac{5}{9} H_{11} \tag{22d}$$

$$\mathscr{D} u_2 = \mathscr{D} u_1 + \tfrac{15}{16} H_2 + \tfrac{5}{24} \Delta t (G_1 + G_2), \tag{22e}$$

$$H_3 = \Delta t F(u_2) - \tfrac{153}{128} H_2, \tag{22f}$$

$$\mathscr{D} u^{n+1} = \mathscr{D} u_2 + \tfrac{8}{15} H_3 + \tfrac{1}{8} \Delta t (G_2 + G^{n+1}), \tag{22g}$$

where $\mathscr{D}=(1-\Delta t^2 A_0^2 \nabla\nabla\cdot)$.

In order to investigate the stability of RK3, we write equation (18) in the form

$$U^{n+1}=BU^n, \tag{23}$$

with

$$B=M(8/15)M(15/16)M(1/3)+M(8/15)N(25/48)+N(51/80)M(1/3)+N(-17/48),$$

where the matrices M and N are given by

$$M(\beta)=\begin{pmatrix} 1 & -\beta\dfrac{\Delta t i k}{\rho}\dfrac{1}{Y} \\ -\beta\Delta t i k \beta\gamma P_0 & 1 \end{pmatrix}, \qquad N(\beta)=1-M(\beta),$$

with $Y=1+\Delta t^2 k^2 A_0^2$. The eigenvalues depend on the parameter $a=A_0/c_s$, with $c_s=(\gamma P_0/\rho_0)^{1/2}$. They all lie within the unit circle for every time step if $a\geq a_c\approx 0{\cdot}574$.

3.2. *The full Navier–Stokes equations*

The RK3 numerical scheme has been implemented for the full Navier–Stokes equations. All but the diffusion terms are handled by the Runge–Kutta scheme and are represented by F in equation (22a). The semi-implicit term $\mathscr{D}$ is used for the two velocity components, which are in turn governed by evolution equations coupled by the second viscosity term. These terms are represented by G in equation (22a) and are treated by a Crank–Nicholson scheme, leading to the following linear system for the unknowns (u^{n+1}, v^{n+1}):

$$\begin{aligned}
&\frac{1}{\xi\Delta t}\widehat{\rho_{\text{tot}}u}_k^{n+1}+(Dt+1)k^2F_x^2\hat{u}_k^{n+1}+Dt\,ikF_x\frac{\partial\hat{v}_k^{n+1}}{\partial z}-\frac{\partial^2\hat{u}_k^{n+1}}{\partial z^2}=\frac{1}{\zeta\Delta t}\widehat{\rho_{\text{tot}}S_{u,k}},\\
&\frac{1}{\xi(Dt+1)}\widehat{\rho_{\text{tot}}v}_k^{n+1}+\frac{Dt}{Dt+1}ikF_x\frac{\partial\hat{u}_k^{n+1}}{\partial z}+\frac{1}{\zeta(Dt+1)}k^2F_x^2\hat{v}_k^{n+1}-\frac{\partial^2\hat{v}_k^{n+1}}{\partial z^2}=\frac{1}{\zeta\Delta t}\widehat{\rho_{\text{tot}}S_{v,k}}.
\end{aligned} \tag{24}$$

In this equation $Dt=A_0^2\Delta t/\zeta+\frac{1}{3}$ and ζ takes successively the values given by the procedure (22), where S_u and S_v are computed from the explicit stage with RK3; the quantity ρ_{tot} is the total density and $\hat{u}_k$ denotes the spectral coefficient of u. This linear system is solved by means of a Chebyshev iterative method:

$$\hat{u}_k^{(j+1)}=\omega_j\hat{u}_k^{(j)}+(1-\omega_j)\hat{u}_k^{(j-1)}-\alpha\omega_j L_{\text{ap}}^{-1}(L_{\text{sp}}\hat{u}_k^{(j)}-S_k), \tag{25}$$

where $\omega_j=2\beta T_j(\beta)/T_{j+1}(\beta)$ and T_j is the Chebyshev polynomial of degree j. The optimal value for a is given by

$$\alpha=\frac{2}{M+m} \quad \text{and} \quad \beta=\min(|1-\alpha m|^{-1}, |1-\alpha M|^{-1}), \tag{26}$$

where m and M are respectively the lower and upper bound of the relevant operator $L_{\text{ap}}^{-1}L_{\text{sp}}$.

Several preconditioning matrices can be built. The simplest one uses the second-order finite difference approximation of the diffusion operator. Write the preconditioning matrix as

$$L_{\text{ap}}=\begin{pmatrix} L_{\text{ap}}^{11} & L_{\text{ap}}^{12} \\ L_{\text{ap}}^{21} & L_{\text{ap}}^{22} \end{pmatrix}, \tag{27}$$

Table I. Spectrum of the operator $L_{ap}^{-1} L_{sp}$ versus the time step and the parameter of the semi-implicit scheme

c	$a = A_0/c_S$	Spectrum
0·10	0·0	[1·00, 1·06]
3·00	0·0	[1·00, 1·41]
3·00	0·5	[1·00, 1·86]

Table II. Iteration number of the u–v- and E-equations versus the time step and the parameter of the semi-implicit scheme

		Iteration number	
c	$a = A_0/c_S$	u–v-equation	E-equation
0·10	0·0	24	11
2·00	0·5	33	13
2·50	0·5	36	15

with

$$L_{ap}^{11} = \frac{\rho(z)}{\alpha \Delta t} + (Dt + 1) k^2 F_x^2 - \frac{\partial^2}{\partial z^2}, \tag{28}$$

$$L_{ap}^{22} = \frac{\rho(z)}{\alpha(Dt + 1)} + \frac{k^2 F_x^2}{\alpha(Dt + 1)} - \frac{\partial^2}{\partial z^2}, \tag{29}$$

$$L_{ap}^{12} = L_{ap}^{21} = 0. \tag{30}$$

The spectrum of the operator $L_{ap}^{-1} L_{sp}$ is given in Table I as a function of the CFL number and the coefficient of the semi-implicit term a. For the last case ($c = 3{\cdot}0$, $a = 0{\cdot}5$) we obtain some complex eigenvalues with imaginary parts of order 10^{-3}.

Table II gives the number of iterations needed to search a residue lower than 10^{-8} for different values of a and c. It turns out that solving the u- and v-equations simultaneously requires roughly twice the number of iterations needed to solve one equation. We also compared the computational efficiency of this numerical scheme with that presented in Reference 7. It appears that a time step of the RK3 requires much more CPU time than the AB2-AM3 numerical scheme, but the time step size is much larger. As a result, the semi-implicit RK3 is only slightly less efficient with regards to computer time, but the accuracy and consistency are much better.

We have also used to finite difference and the spectral approximation of the first derivative for L_{ap}^{12} and L_{ap}^{21}. In both cases the spectrum is not shrunk and therefore leads to the same rate of convergence.

4. NUMERICAL APPLICATIONS

As an example of the numerical procedure described in Section 3, we have computed convection solutions for different Stefan number values, i.e. for different values of the stratification parameter.

In the following we detail the features of these solutions and compare them with those obtained with a constant heat flux or fixed temperature at the two boundaries.[9,11] In our simulations the aspect ratio is 4 and the Rayleigh number 11 500 for all cases. The Prandtl number is $Pr=0{\cdot}1$ and the ratio of specific heats is that of a monatomic gas, $\gamma=1{\cdot}67$. The polytropic index is equal to the value $m=1$.

As opposed to the cases already investigated,[7,9,11] the convection solutions with a Robin boundary condition for the temperature seem to be more symmetrical, as seen in Figures 1 and 2. Indeed, the centres of the rolls are located at $x=1{\cdot}06$, $z=0{\cdot}62$ and $x=1{\cdot}08$, $z=0{\cdot}66$ for the cases corresponding to Stefan numbers 1 and 2·73 respectively. The centre is only slightly shifted towards the downward-directed plume and more clearly below the middle of the layer even in the case where density and pressure fluctuations are very high with respect to the basic state. Both shifts evolve weakly when the Stefan number is increased. In that respect it is of interest to compare the widths of rising and sinking flows defined by the point where the velocity is halved.[9] The width of the upflow is 0·45 while the downflow extends to 0·32 for $S_f=1$. The asymmetry increases for the $S_f=2{\cdot}73$ case, where the widths are respectively 0·32 and 0·21. Consequently the velocities at the two boundaries are not really different: the value of the velocity is 398 arbitrary units (a.u.) at the upper boundary and -485 a.u. at the lower one for $S_f=1$, and 331 and 426 a.u. respectively for $S_f=2{\cdot}73$.

According to this weak asymmetry, the maximum Mach number increases with the Stefan number. Beyond an approximate value of 2 the steady flow exhibits some supersonic regions concentrated near the upper bound.

Table III gives the final steady values of characteristic quantities such as the maxima of the velocity, the Mach number and the relative thermodynamical fluctuation quantities. The Mach number is defined by $(u^2+v^2)/c_s$, where c_s is the local sound speed. The root-mean-square (RMS) value of ϕ is defined by

$$\|\phi\|=(\bar{\phi}^2)^{1/2}.$$

The maximum velocity is horizontally directed and occurs at the lower boundary of the layer approximately below the centres of the rolls for all cases. The maximum vertical velocity occurs in the downward-directed plume at the same altitude ($z\simeq 0{\cdot}63$ for all values of Stefan number except $S_f=1$, where $z\simeq 0{\cdot}58$) as the centres of the rolls. The vertical velocity increases with the

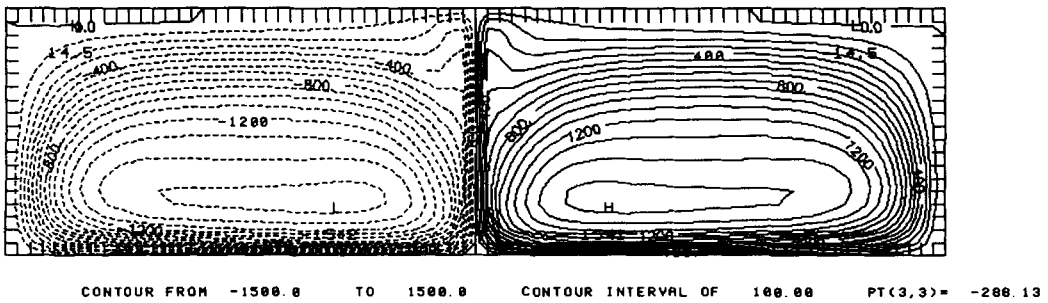

Figure 1. Iso-vorticity contours for a Stefan number equal to 1. The aspect ratio is 4, the Rayleigh number is 11 500, the polytropic index is 1, the Prandtl number is 0·1 and the ratio of specific heats is 1·67. A weak asymmetry of the flow appears, although the iso-vorticity contours reveal strong velocity gradients at the bottom of the layer. The number of grid points is $N=150$, $M=30$

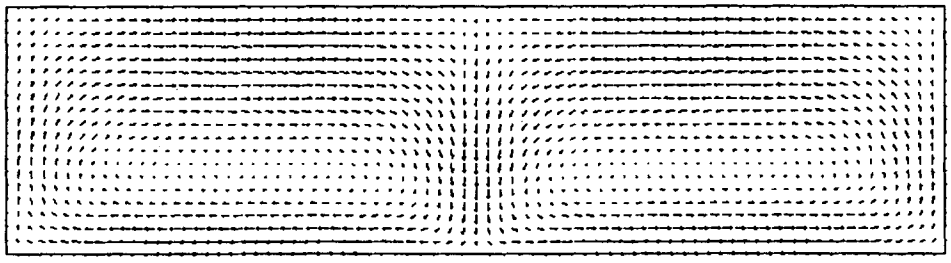

(a)

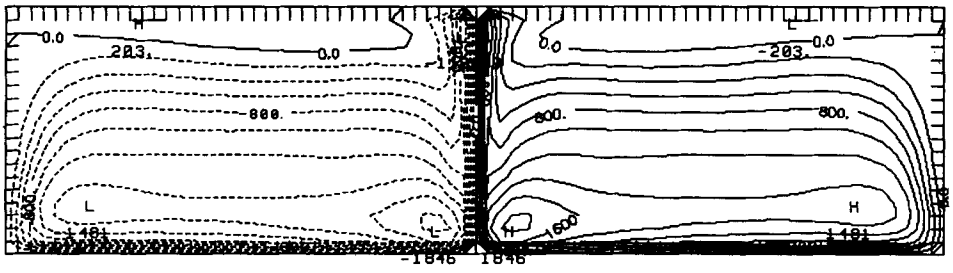

(b)

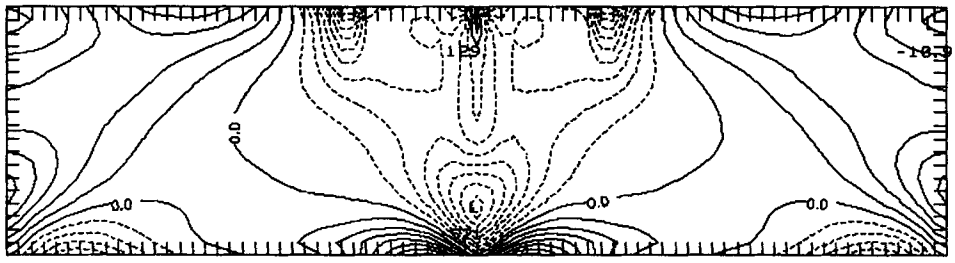

(c)

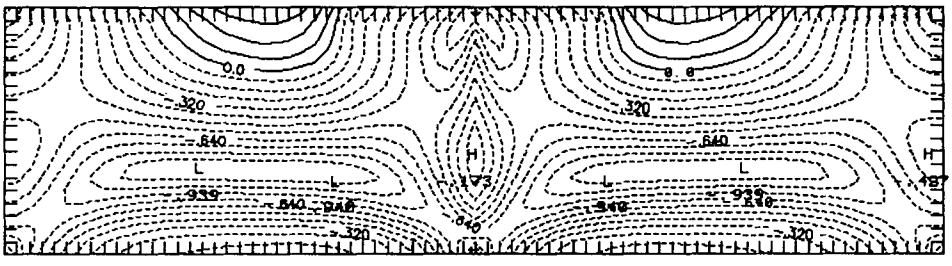

(d)

Figure 2. (a) Velocity field, (b) iso-vorticity contours and (c) velocity divergence contours for a Stefan number equal to 2·73. The velocity field divergence is positive when the fluid expands (i.e. in the rising flow) and negative when it is compressed (i.e. in the sinking flow). (d) Iso-values of the Mach number minus one; supersonic regions appear clearly at the top of the layer. The number of grid points is $N = 150$, $M = 30$

Table III. Characteristics of the solutions for different values of the Stefan number

Characteristic	Stefan number				
	1·0	1·5	2·0	2·5	2·73
ρ_1/ρ_2	2	2·5	2·0	3·5	3·73
P_1/P_2	4	6·25	9	12·25	13·91
Maximum velocity	$4{\cdot}866\times10^2$	$4{\cdot}777\times10^2$	$4{\cdot}606\times10^2$	$4{\cdot}387\times10^2$	$4{\cdot}300\times10^2$
Horizontal velocity	$4{\cdot}866\times10^2$	$4{\cdot}777\times10^2$	$4{\cdot}606\times10^2$	$4{\cdot}387\times10^2$	$4{\cdot}300\times10^2$
$\|\|u\|\|$	$2{\cdot}304\times10^2$	$2{\cdot}286\times10^2$	$2{\cdot}232\times10^2$	$2{\cdot}149\times10^2$	$2{\cdot}104\times10^2$
Vertical velocity	$3{\cdot}122\times10^2$	$3{\cdot}352\times10^2$	$3{\cdot}409\times10^2$	$3{\cdot}355\times10^2$	$3{\cdot}303\times10^2$
$\|\|v\|\|$	$1{\cdot}077\times10^2$	$1{\cdot}027\times10^2$	$0{\cdot}971\times10^2$	$0{\cdot}910\times10^2$	$0{\cdot}881\times10^2$
Maximum momentum	$9{\cdot}316\times10^2$	$1{\cdot}097\times10^2$	$1{\cdot}249\times10^2$	$1{\cdot}394\times10^2$	$1{\cdot}462\times10^2$
$\|\|\rho v\|\|$	$3{\cdot}884\times10^2$	$4{\cdot}509\times10^2$	$5{\cdot}040\times10^2$	$5{\cdot}465\times10^2$	$6{\cdot}628\times10^2$
Nusselt number	1·821	2·424	3·056	3·691	3·992
Maximum Mach number	0·550	0·789	1·170	1·228	1·315
ρ_{max}	0·217	0·536	1·054	1·941	2·700
$\|\|\rho'/\bar{\rho}\|\|$	0·063	0·112	0·168	0·226	0·255
T_{max}	0·174	0·269	0·365	0·457	0·496
$\|\|T'/\bar{T}\|\|$	0·074	0·101	0·124	0·143	0·150
P_{max}	0·324	0·654	1·076	1·536	1·756
$\|\|P'/\bar{P}\|\|$	0·101	0·180	0·266	0·351	0·388

stratification for subsonic solutions. When the supersonic regions appear, the vertical velocity decreases with increasing value of the Stefan number.

The maximum Mach number based on the flow velocity occurs at the upper boundary of the layer where the velocity is horizontal. It increases from 0·55 to 1·315 with increasing value of the Stefan number. Figure 3(d) displays the iso-values of the Mach number in excess of unity, showing clearly the supersonic domain at the upper boundary of the layer. Similar behaviour has been found by Yamaguchi[11] in the case of a fixed heat flux.

The maxima of the thermodynamical variables given in the Table III are defined by the relation

$$\rho_{max} = \max \frac{\rho(x, z)}{\bar{\rho}(z)}, \tag{31}$$

where the maximum is taken over the two-dimensional domain. The maxima of the relative density fluctuation ρ_{max} range from 0·217 to 2·7 when the Stefan number reaches the value 2·73 (Figure 4). Except for the case $S_f = 1$, this maximum is located at the upper boundary of the layer above the sinking flow. The maximum of the relative temperature fluctuations arises obviously in the rising flow very close to the lower boundary (Figure 5). The maximum of the pressure, also defined by equation (31), reflects the very high values of the density fluctuations for the supersonic cases (Figure 6).

Beyond this value of the Stefan number, the peak of the density fluctuations is too high and cannot be resolved by the numerical scheme without some artificial viscosity.

In steady state the total energy flux becomes independent of depth and is written as[9, 11]

$$F_T = F_c + F_K + F_R + F_V, \tag{32}$$

where F_c is the convective heat flux, F_K is the kinetic flux, F_R is the radiative flux and F_V is the

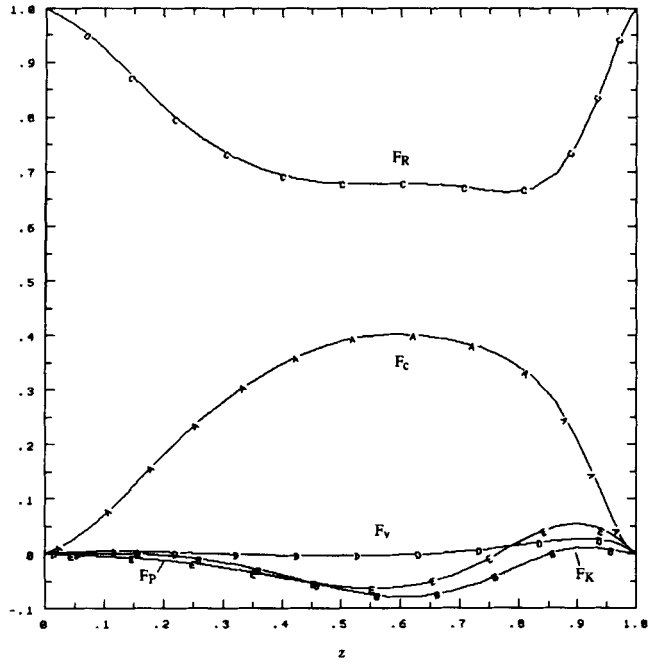

(a)

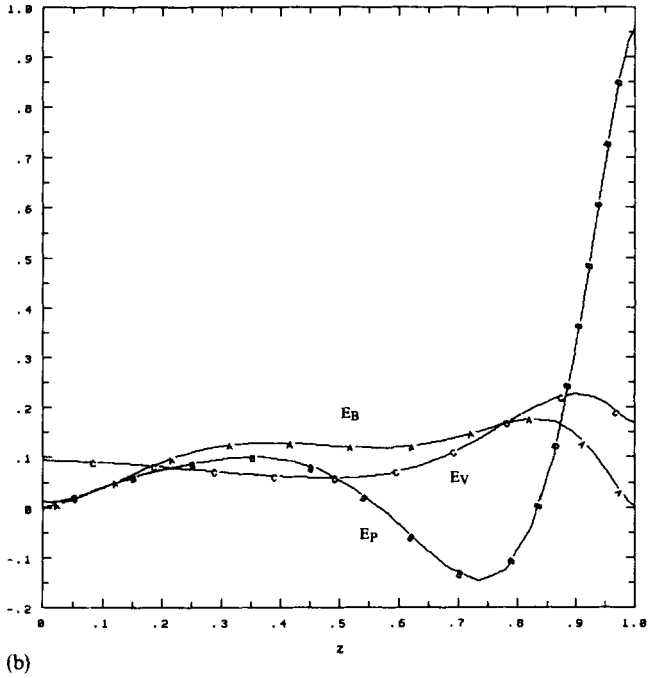

(b)

Figure 3. (a) Convective heat (F_c), kinetic (F_K), radiative (F_R), viscous (F_V) and pressure (F_P) fluxes and (b) work done by buoyancy (E_B), pressure (E_P) and viscous (E_V) forces versus the altitude z for the same set of parameter values used in Figure 1. Fluxes and work have been scaled by the total flux at the bottom. The co-ordinate z varies from 0 to 1 from top to bottom

viscous flux defined by the following relations:

$$F_c = \overline{-\rho C_p u_2 T'}, \tag{33}$$

$$F_K = -\tfrac{1}{2}\overline{\rho u_i u_i u_2}, \tag{34}$$

$$F_R = K\frac{\partial \bar{T}}{\partial z}, \tag{35}$$

$$F_V = \overline{u_i \sigma_{2i}}, \tag{36}$$

where the overbar denotes the horizontal average and the prime stands for the fluctuation about this mean.

We also define the pressure flux by $F_P = \overline{u_2 P'}$ and the rates of work done by buoyancy, pressure and viscous forces, which are given by

$$E_B = g\overline{\rho u_2}, \tag{37}$$

$$E_P = \overline{P'\frac{\partial u_i}{\partial x_i}}, \tag{38}$$

$$E_V = \overline{\sigma_{ij}\frac{\partial u_i}{\partial x_j}}. \tag{39}$$

Table IV gives the maxima of the different fluxes contributing to the total flux and of the work done by gravitational forces, pressure fluctuations and viscous forces. The evolutions with respect to z are reported in Figures 3 and 7, where all quantities have been scaled to the total flux at the bottom.

For a Stefan number equal to 1 the main contribution to the total flux is given by the radiative flux, which is approximately constant at 70% of the total flux between $z = 0{\cdot}4$ and $0{\cdot}8$. Recall that the expression of the adiabatic flux is given by the condition $dS = 0$, where S is the entropy of the fluid, which leads to $F_a = gK/C_p$.[16] Between $z \simeq 0{\cdot}6$ and $0{\cdot}9$ the radiative flux is approximately equal to the adiabatic flux so that the heat transfer is maximum. It turns out that for large enough temperature gradients a hydrodynamical motion is created in order to maximize the heat transport.

Table IV. Maximum values for the heat, kinetic, radiative, viscous and acoustic fluxes, and maxima of the work done by gravitational forces, pressure fluctuations and viscous forces

Maximum	Stefan number				
	1·0	1·5	2·0	2·5	2·73
Heat flux	$0{\cdot}339 \times 10^7$	$0{\cdot}334 \times 10^2$	$0{\cdot}337 \times 10^2$	$0{\cdot}334 \times 10^2$	$0{\cdot}332 \times 10^2$
Kinetic flux	$-0{\cdot}659 \times 10^6$	$-0{\cdot}992 \times 10^6$	$-0{\cdot}107 \times 10^6$	$-1{\cdot}162 \times 10^6$	$-1{\cdot}150 \times 10^6$
Radiative flux	$0{\cdot}843 \times 10^7$	$0{\cdot}620 \times 10^7$	$0{\cdot}510 \times 10^7$	$0{\cdot}444 \times 10^7$	$0{\cdot}423 \times 10^7$
Viscous flux	$0{\cdot}227 \times 10^6$	$0{\cdot}273 \times 10^6$	$0{\cdot}294 \times 10^6$	$0{\cdot}294 \times 10^6$	$0{\cdot}289 \times 10^6$
Acoustic flux	$-0{\cdot}537 \times 10^7$	$-0{\cdot}706 \times 10^6$	$-0{\cdot}825 \times 10^6$	$-0{\cdot}859 \times 10^6$	$-0{\cdot}853 \times 10^6$
Gravitational force work	$0{\cdot}150 \times 10^7$	$0{\cdot}174 \times 10^7$	$0{\cdot}190 \times 10^7$	$0{\cdot}195 \times 10^7$	$0{\cdot}175 \times 10^7$
Pressure fluctuation work	$0{\cdot}808 \times 10^7$	$0{\cdot}115 \times 10^8$	$0{\cdot}146 \times 10^8$	$0{\cdot}168 \times 10^8$	$0{\cdot}175 \times 10^8$
Viscous force work	$0{\cdot}191 \times 10^7$	$0{\cdot}217 \times 10^7$	$0{\cdot}228 \times 10^7$	$0{\cdot}228 \times 10^7$	$0{\cdot}225 \times 10^7$

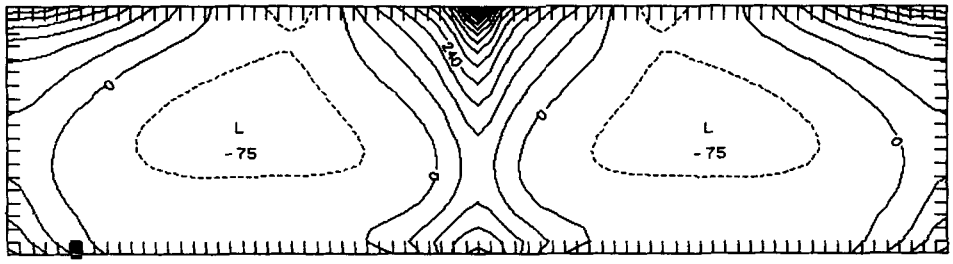

(a)

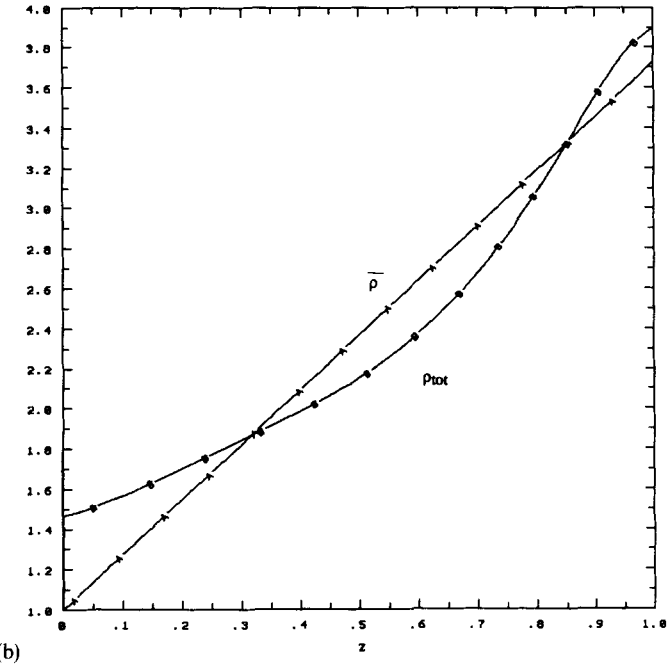

(b)

Figure 4. (a) Relative density fluctuation contours for $S_f = 2{\cdot}73$. Minima of the relative density fluctuations occur at the centres of the rolls. The maximum, equal to $2{\cdot}7\ \bar{\rho}(Z^{-1})$, occurs at the upper boundary in the sinking flow. (b) Static and total density profiles averaged in the x-direction

The heat flux reaches 40% of F_T at $z = 0{\cdot}6$ and vanishes at the two boundaries owing to the Dirichlet boundary conditions used for the velocity. The kinetic flux is negative in the upper region of the layer with a minimum at $z = 0{\cdot}6$ and becomes positive at $z = 0{\cdot}82$; in this region it reaches 3% of F_T. The viscous flux is negative in the middle of the layer between $z = 0{\cdot}31$ and $0{\cdot}63$. It is maximum at $z = 0{\cdot}90$–$0{\cdot}95$ with a value of 2·7% of F_T. The acoustic flux is negative in the upper region of the layer, becomes positive at $z = 0{\cdot}76$ and reaches 10% of F_T in the lower region. The work done by gravitational forces is positive across the layer. Notice that the work done by pressure fluctuations is exactly zero for an incompressible flow; in our case it is positive in the upper part of the layer and negative from $z = 0{\cdot}83$ to the bottom of the layer. It reaches high values

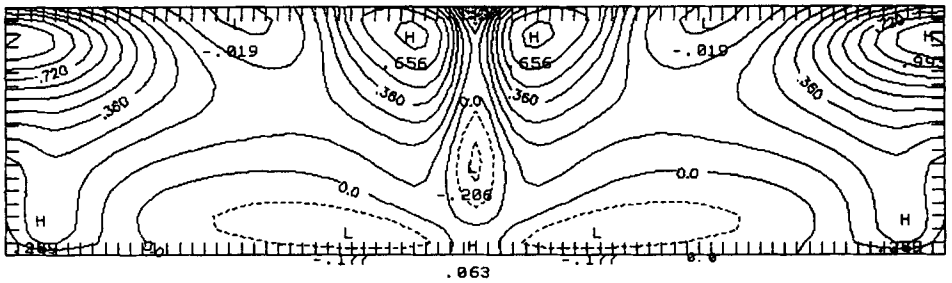

(a)

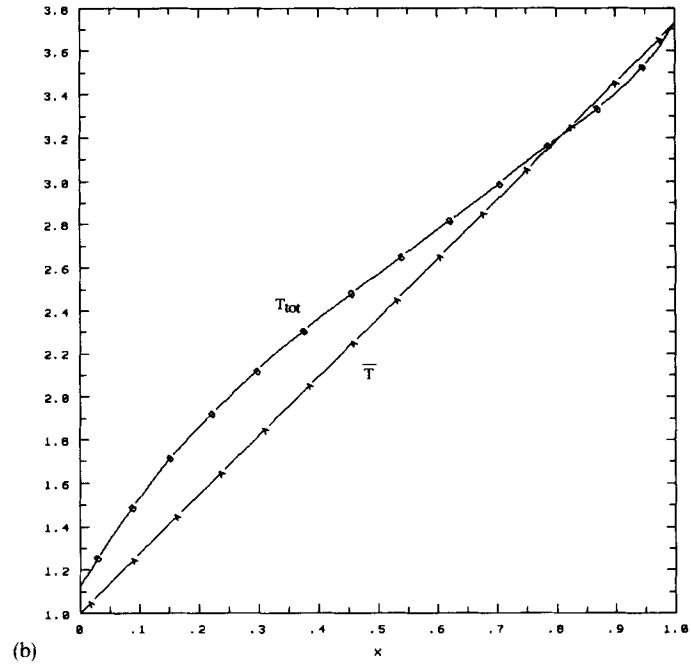

(b)

Figure 5. (a) Relative temperature fluctuation contours for $S_f = 2{\cdot}73$. A maximum of 49·6% of the static state value occurs at the upper boundary in the rising flow. (b) Static and total temperature profiles averaged in the x-direction

at the bottom of the layer where pressure fluctuations are large and velocity gradients strong. The work done by the viscous forces does not vanish at the boundaries owing to the free slip boundary conditions used for the velocity.

For a higher stratification parameter value ($S_f = 2{\cdot}73$) the heat flux is now 80% of the total flux at $z = 0{\cdot}7$ and is approximately constant between $z = 0{\cdot}6$ and 0·9. The radiative flux reaches 55% of F_T between $z = 0{\cdot}6$ and 0·9. The acoustic flux is negative in the upper part of the layer, decreases down to -25% of F_T and becomes positive at $z = 0{\cdot}88$. The work done by gravitational forces is always positive and the work done by pressure fluctuations reaches a peak value at the lower boundary owing to a high velocity divergence where the flow meets the boundary.

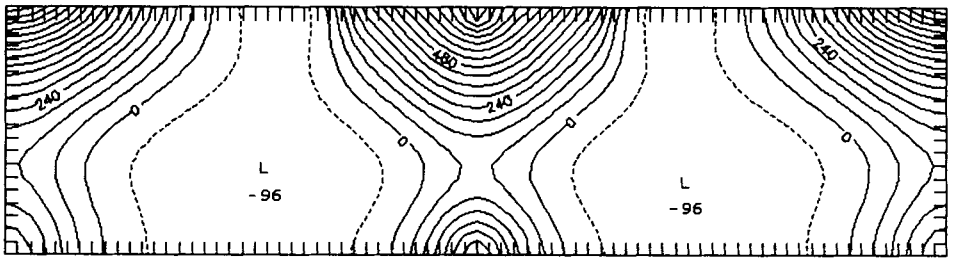

(a)

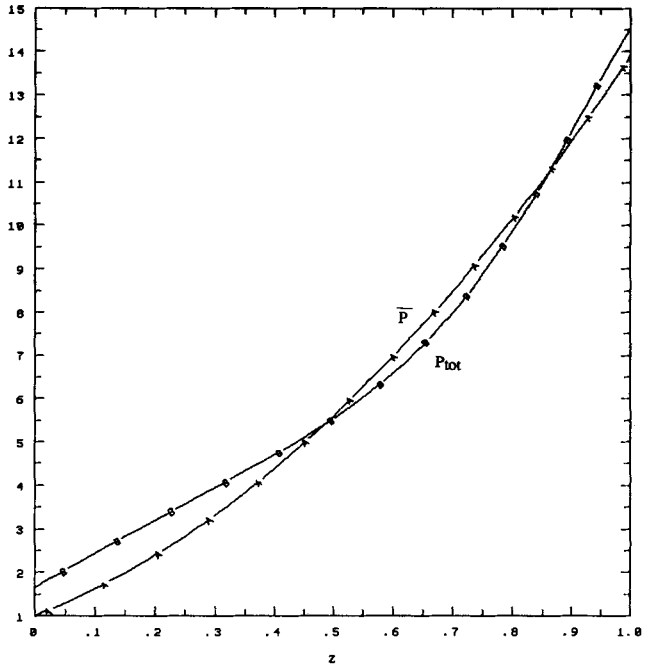

(b)

Figure 6. (a) Relative pressure fluctuation contours for $S_f = 2{\cdot}73$. A maximum of 176% of the static state value occurs at the upper boundary in the rising flow. (b) Static and total pressure profiles averaged in the x-direction. The pressure fluctuations exhibit maxima wherever the flow is changing direction, while weak gradients can be seen in the centres of the rolls

5. CONCLUSIONS

We have developed a pseudo-spectral algorithm to simulate the thermal convection of a two-dimensional fully compressible viscous fluid. Variables are expanded over a Fourier basis in the horizontal direction and over Chebyshev polynomials in the vertical inhomogeneous direction. A third-order Runge–Kutta numerical scheme and a semi-implicit treatment of the convective terms have been used. All diffusion terms are handled with the Chebyshev iterative method in the Fourier space. The fluid is a perfect gas with constant dynamic viscosity and thermal conductivity. Both sub- and supersonic steady state solutions have been reached with a Robin boundary

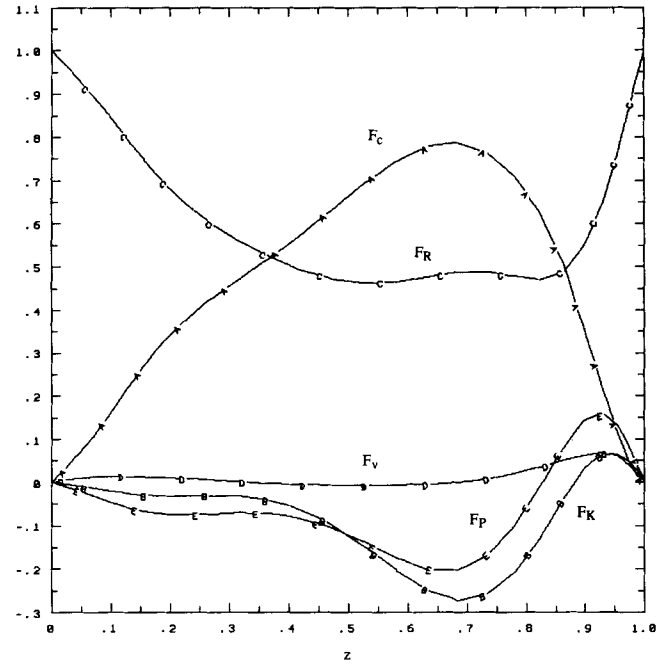

(a)

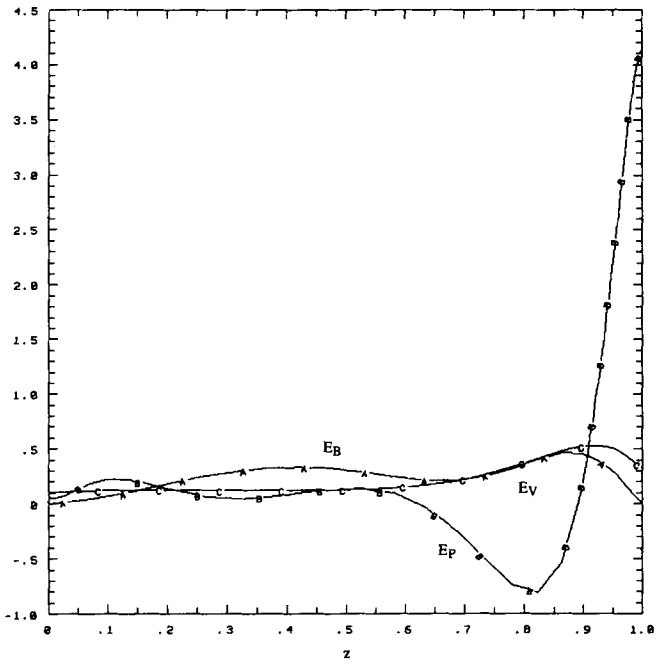

(b)

Figure 7. (a) Convective heat (F_c), kinetic (F_K), radiative (F_R), viscous (F_V) and pressure fluxes and (b) work done by buoyancy (E_B), pressure (E_P) and viscous (E_V) forces versus the altitude z for a Stefan number equal to 2·73. Fluxes and work have been scaled by the total flux at the bottom. The co-ordinate z varies from 0 to 1 from top to bottom

condition for the temperature. They reveal the features of compressible convection even in the case of a moderate value of the stratification parameter.

ACKNOWLEDGEMENTS

I would like to thank M. Meneguzzi for pointing out Reference 14. I also thank G. Zerah for setting up the NCAR graphics package at Limeil. NCAR is supported by NSF. Computations have been carried out on a CRAY 1-S running under UNICOS.

APPENDIX: NOMENCLATURE

ρ	density
u_i	velocity component
P	pressure
T, θ	temperature
σ	stress
t	time
x, z, x_i	space co-ordinates
g	gravitation
E	total energy
e	internal energy
δ	Kronecker symbol
μ	viscosity
R_*	gas constant
K	thermal conductivity
S_f	Stefan number
Z	stratification
m	polytropic index
β_0/d	temperature gradient
A	aspect ratio
Pr	Prandtl number
γ	ratio of specific heats
Ra	Rayleigh number
A_0	parameter of the semi-implicit scheme
L_{sp}	spectral approximation of the operator L
L_{ap}	perconditioning of the operator L
α, β	parameters of the Chebyshev iterative method
F_c	convective heat flux
F_K	kinetic flux
F_R	radiative flux
F_V	viscous flux
E_B	rate of work done by buoyancy
E_P	rate of work done by pressure forces
E_V	rate of work done by viscous forces

REFERENCES

1. C. Canuto, M. Y. Hussaini, A. Quarteroni and T. A. Zang, *Spectral Methods in Fluid Dynamics*, Springer, New York, 1988.

2. T. A. Zang, C. L. Streett and M. Y. Hussaini, 'Spectral methods for CFD', *ICASE Report No. 89-13*, 1989.
3. T. Passot and A. Pouquet, *J. Comput. Phys.*, **75**, 300, 313 (1988).
4. G. Erlebacher and Y. M. Hussaini, *Appl. Numer. Math.*, in the press.
5. S. Bonazzola and J. A. Marck, 'Three-dimensional gas dynamics in a sphere', *Preprint*, Observatoire de Meudon, 1988.
6. K. Dang and P. Loisel, 'Direct simulation of viscous compressible transitional flows', *ONERA Report No. 1987-23*, 1987.
7. S. Gauthier, *J. Comput. Phys.*, **75**, 217 (1988).
8. E. Graham, *J. Fluid Mech.*, **70**, 689 (1975).
9. N. E. Hurlburt, J. Toomre and J. Massaguer, *Astrophys. J.*, **282**, 557 (1984).
10. K. L. Chan and C. L. Wolff, *Astrophys. J.*, **263**, 935 (1982).
11. S. Yamaguchi, *Publ. Astron. Soc. Japan*, **37**, 735 (1985); **36**, 613 (1984).
12. P. R. Woodward, D. H. Porter, K. H. A. Winkler and N. J. Zabusky, 'Simulations of unstable fluid flow using the piecewise-parabolic-method (PPM)', *Preprint*, 1987.
13. D. Gottlieb and S. A. Orszag, *Numerical Analysis of Spectral Methods: Theory and Applications*, CBMS–NSF Regional Conferences Series in Applied Mathematics, SIAM, Philadelphia 1977.
14. D. S. Harned and W. Kerner, *J. Comput. Phys.*, **60**, 62–75 (1985).
15. J. H. Williamson, *J. Comput. Phys.*, **35**, 48–56 (1980).
16. L. D. Landau and E. M. Lifshitz, *Fluid Mechanics*, Pergamon, Oxford, 1959.